Biomass-derived carbon/γ-MnO_2 nanorods/S composites prepared by facile procedures with improved performance for Li/S batteries

Fernando Luna-Lama, Celia Hernández-Rentero, Alvaro Caballero*, Julián Morales[+]

Dpto. Química Inorgánica e Ingeniería Química, Instituto de Química Fina y Nanoquímica, Universidad de Córdoba, 14071 Córdoba, Spain

*Corresponding author: alvaro.caballero@uco.es (+34 957 21 86 20)

[+]Co-author: iq1mopaj@uco.es (+34 957 21 86 21)

Highlights

- A biomass-activated carbon from olive stone with nanorod γ-MnO_2-S is reported.
- Facile and low-cost processes were used to improve the practical applications.
- Composites were studied for application as a cathode for Li/S batteries.
- γ-MnO_2 in the C/S composite markedly improves the performance of the batteries.
- The γ-MnO_2 nanorods confine the polysulphides, restricting their dissolution.

Abstract

The promising prospects of the Li/S battery, due to its theoretical energy density of about 2500 Wh kg^{-1}, are severely limited by two main weaknesses: the poor conductivity of S and the solubility of the polysulphides in the electrolyte. A combination of carbon and transition metal oxides is the best option for mitigating both of these shortcomings simultaneously. In this work, we use hydrothermally-tailored γ-MnO_2 nanorods combined with an activated biomass-derived carbon, which is an inexpensive material and easy to prepare. This strategy was also followed for a AC/MnO_2/S composite, a preparation of which was made by grinding; this is the simplest method for practical applications. More complex procedures for the formation of in situ hydrothermal MnO_2 nanorods gave similar results to those obtained from grinding. Compared with the AC/S composite, the presence of MnO_2 markedly increased the delivered capacity and improved the cycling stability at both low (0.1 C) and high (1 C) currents. This behaviour results from a combination of two main effects: firstly, the MnO_2 nanorods increase the electrical conductivity of the electrode, and secondly, the small particle size of the oxide can enhance the chemisorption properties and facilitate a redox reaction with polysulphides, more efficiently blocking their dissolution in the electrolyte.

Keywords: biomass-derived carbon; manganese dioxide; composites; lithium-sulphur batteries

1. Introduction

Today, Li-ion batteries (LIB) play a significant role in various fields, and particularly in portable electronic devices, laptops, mobile phones and digital cameras. The main reasons for this are their low weight, a specific energy that is adequate for the demands of these devices and a reasonably long life [1-3]. Unfortunately, their ability to meet the demands of the operation of other emerging technologies, such as electric vehicles and electrochemical storage energy devices for renewable power systems, is questionable, as these devices require higher energy values (around 200 Wh kg^{-1}) than those supplied by LIBs [2,4]. Alternative reversible electrochemical reactions in which the electron transfer is greater than that taking place in an LIB (which has a maximum of one electron) may be able to overcome this shortcoming, as a reaction-based battery would supply a higher specific capacity and hence a higher specific energy.

The electrochemical reaction between Li and S satisfies the above condition, and its theoretical specific capacity and specific energy are 1675 mA h g^{-1} and 2600 Wh kg^{-1}, respectively (much higher than that of the current Li-ion battery, which is around 600 Wh kg^{-1}). Moreover, S is an abundant element, and is cheap and environmentally friendly. Despite these advantages, the Li/S battery has several drawbacks that hinder its use in practical applications [5-8]. The three most important of these are [8,9]: (i) the low electronic conductivity of S and its discharge product Li_2S, ~ 5×10^{-30} and ~ 10^{-14} S cm^{-1}, respectively, several orders of magnitude lower than that of a transition metal oxide-base electrode, giving rise to a low use of the active material as a result; (ii) the significant volumetric expansion/shrinkage (approx. 80%) during the discharge/charge processes due to the different densities of S and Li_2S (2.03 and 1.67 g cm^{-3}, respectively) causes structural instability of the electrode; and (iii) the solubility of the intermediate lithium polysulphides (LiPSs) in the liquid electrolyte creates a “shuttle effect”, which causes capacity loss of the cell on cycling and the corrosion of the Li electrode [10].

A common technique for mitigating these obstacles is the use of additives of various compositions. Carbon is one of the more promising additives, as it can have a positive effect on the three drawbacks mentioned above. Its good conductivity can counteract the insulating behavior of S; it can also buffer the strains produced by the volume changes involved in the S ↔ Li_2S conversion; and finally, it can trap the polysulphides in its pore system, thus alleviating the shuttle effect [11]. This multifaceted behavior is the reason for the abundant literature on carbon materials of diverse textural and morphological properties as sulphur hosts [12]. Since the adsorption of LiPSs is mainly related to the surface area and porosity, the textural properties of carbon play a relevant role. In this context, activated carbons (AC), which have a well-defined micropore system that enhances their adsorption properties, are a good choice [13]. However, the nonpolar properties of carbon weaken the interactions with polar species of LiPS. This feature suggests an alternative approach to constraining the diffusion of polysulphides based on polar compounds, involving metal oxides [14]. Ti- and Mn-based oxides have been most widely studied as possible components of the S composite; these have been used alone [15-18] and have been frequently combined with graphitic carbons [18-22]. It should be mentioned that the interest aroused by Mn oxides is probably motivated by the variety of phases and valence states, combined with the non-toxic behavior and abundance of the element [23]. In the last few years, several C/MnO_2/S composites have been studied as electrodes for Li/S batteries, showing disparate levels of performance [23-35]. The specific capacity values range from 1125 to 400 mAh g^{-1} after 100 cycles at 0.2 C and 0.1 C, respectively. The reason for this is that the numerous factors affecting the performance of a battery make it difficult to establish comparisons, even between systems using materials of a similar nature. In most of these articles, the main focus is the shape and morphology of the carbon particles (nanofibres, nanotubes, nanosheets, hollow spheres, etc.), the synthesis of which require complex and laborious procedures, either using hard templates or special methodologies for obtaining particular morphologies. For S, the most frequently used deposition method is melt-diffusion, involving heating in a vacuum or inert atmosphere at temperatures above 150ºC; other deposition methods, such as dissolving S in CS_2, pose serious problems with regard to solvent management. These factors mean that these proposals are very expensive and have uncertain feasibility for practical applications on a large scale.

In this context, the use of biomass as a source of C, well known in the manufacture of ACs [36], is gaining relevance in the field of electrochemical storage energy [37], and particularly as source of a C host for Li/S batteries [38-42]. Biomass-derived carbons possess a notable property, which is the ability to induce a pore system during preparation; this is beneficial for sulphur deposition and for capturing the LiPSs in the cavities to mitigate the shuttle effect. In this study, we use a microporous carbon obtained from olive pits, combined with MnO_2 nanorods prepared using a hydrothermal process, and examine its electrochemical properties as an electrode for Li/S batteries. AC/MnO_2/S composites are prepared using simple and straightforward procedures, a requisite for developing low-cost and sustainable Li/S batteries for future applications.

2. Material and methods

2.1 Synthesis of activated carbon and MnO_2

The olive stone AC was obtained from the bioenergy plant at S.C.O. El Tejar, Córdoba (Spain); details of its synthesis are described elsewhere [43]. MnO_2 was obtained using a hydrothermal method, following the procedure proposed by Gu et al. [44]. In a typical procedure, $MnSO_4 \cdot H_2O$ (Panreac, 51 mmol) and $(NH_4)_2S_2O_8$ (Panreac, 51 mmol) were dissolved in 260 mL of deionised water; the solution was distributed to four Teflon-lined stain-less steel autoclaves (VEVOR, 80 mL) and further heated at 90ºC for 6 h. The resultant solid was filtered, washed with distilled water and absolute ethanol several times and dried in a oven at 80ºC. The chemical reaction in (1) achieved a yield of 74%:

$$MnSO_4{\cdot}H_2O + (NH_4)_2S_2O_8 + H_2O \rightarrow MnO_2 + (NH_4)_2SO_4 + 2\ H_2SO_4 \quad (1)$$

2.2 Synthesis of AC/S@gr; AC/MnO_2/S@gr; AC/MnO_2/S@ht composites

Commercial micronized S (Solvay) was used for the three composites studied, which had an initial S content of 60% (w/w). The remaining 40% was made up either of AC or a mixture of AC and MnO_2 in a 1:1 mass ratio. Two composites were prepared by grinding for 3 h at 300 rpm in ethanol in a Retsch PM100 ball mill. These composites are identified by the letters "gr". The third composite, identified by the letters "ht", was prepared using an AC matrix together with the chemical precursors of MnO_2, which were placed in a Teflon-lined stainless autoclave and underwent the treatment described above for the synthesis of pure oxide. In this case, the S in the composite was homogeneously dispersed by magnetic stirring in ethanol for 14 min at 4000 rpm, using a Ultraturrax IKA T18. These conditions were chosen to be comparable to those used in the grinding method. The scheme shown in Fig. 1 summarises the different steps used for the preparation of the composites.

Figure 1

2.3. Carbon, MnO_2 and composite characterisation

The structural properties were examined using X-ray diffraction (XRD) and X-ray photoelectron spectroscopy (XPS). The XRD patterns were recorded with a Bruker D8 Discover X-ray diffractometer, using Cu Kα radiation and a Ge monochromator. The XPS spectra were obtained on a SPECS mod. PHOIBOS 150 MCD spectrometer, using monochromatic Mg Kα radiation and a multichannel detector. All spectra were fitted to Gauss–Lorentz curves to better identify the different chemical environment of the elements in each material. The morphology of the samples and the element mapping were investigated using a Jeol JSM-7800F scanning electron microscope (SEM) equipped with a with an X-ACT Cambridge Instrument analyser. The specific surface area was determined with a Micromeritics ASAP 2020, using N_2 gas as an adsorbate. Pore size distribution was calculated using the density functional theory (DFT) method, applied to the adsorption branch of the isotherms. The sulphur content was determined by thermogravimetric analysis with a Mettler Toledo TGA/DSC at a heating rate of 5ºC min^{-1} from 25° to 800ºC, in a nitrogen atmosphere.

2.4 Electrode preparation

The positive electrodes were prepared by mixing the composites with PVDF (6020, binder, Solvay) and carbon Super P (conducting agent, Timcal) in a weight proportion of 80:10:10, adding 1-methyl-2-pyrrolidone (Sigma Aldrich, 0.5 mL per 100 mg) and magnetically stirring for 24 h. The resulting slurry was coated using doctor-blade deposition onto an Al foil (thickness 15 μm). The deposits were dried for 24 hours in an oven at 60°C and cut into 12.8 mm discs. The electrodes were then dried in a vacuum overnight at 45ºC. The sulfur loading was appximately 1.0 mg cm^{-2}.

2.5. Cell assembly and electrochemical characterisation

Electrochemical measurements were performed on CR2032 coin cells assembled inside an Ar-filled glovebox (MBraun, oxygen and moisture content lower than 1 ppm) with Li metal foil as a counter and reference electrode. The separator was a polyethylene membrane (Celgard) with a thickness of 25 μm and a porosity of 39%. The electrolyte was LiTFSI (1M, Sigma Aldrich) and $LiNO_3$ 0.4 M (Sigma Aldrich) in 1,3-dioxolane (DOL, Sigma Aldrich) and 1,2-dimethoxyethane (DME, Sigma Aldrich) (1:1 v/v). The cyclic voltammograms (CV) were recorded with a Solartron 1286 at 0.1 mV s^{-1} between 1 and 3 V. Electrochemical impedance spectroscopy (EIS) was carried out using an Autolab (Ecochemie, Pgstat 30) electrochemical workstation in the frequency range 0.1 Hz to 500 KHz at a disturbance amplitude of 10 mV. Galvanostatic measurements were performed on an Arbin BT2143 in a voltage range of 1.8 to 2.7 V at various currents (1 C is defined as 1675 mA g^{-1}). All specific capacity values were calculated per gram of sulphur.

3. Results and discussion

The XRD patterns of activated carbon and the Mn oxide obtained by hydrothermal treatment are shown in Fig. S1 (in the Supplementary Information). The latter pattern can be indexed in the γ-MnO_2 phase (JCPDS 44-0142). The peak weakness and the background of the pattern reveals the formation of a phase of high structural disorder (some reflections as (120) and (003) are not well resolved) [45]. The pattern for activated carbon (Fig. S1b) also exhibits weak, wide peaks at 25° and 43.5° (2θ); these were assigned to the (002) and (100) crystallographic planes, respectively, and are typical of highly disordered carbons. The patterns of the three composites were quite similar, and as an example, the pattern of the AC/MnO_2/S@ht composite is shown in Fig. S1c. The only clearly distinguishable phase was S, which maintained its crystalline structure throughout the treatment to which it was subjected. Neither AC nor MnO_2 were detected, due to their lower content and particularly their low crystallinity.

The three composites were further characterised by XPS. The C 1s spectrum of the AC/MnO_2/S@ht composite is shown as representative sample in Fig. 2a, and was fitted to four components, ascribed to C-C/C=C (283.6 eV), C-O (285.1 eV), C=O (286.5 eV), and O-C=O (287.9 eV) [46]. The percentages of these components are shown in Table 1. In general, the intensity of the peaks assigned to functional oxygen groups increased slightly for the composites with MnO_2. The S 2p spectrum, as shown in Fig. 2 b, is characterised by the S doublet ($2p_{3/2}$ and $2p_{1/2}$) with energies of 162.7 eV and 164 eV respectively, and a lower intensity peak at higher energies (at 167.2 and 168.4 eV, respectively) is assigned to S bound to O, derived from its oxidation [47]. In fact, the intensity of this peak increases when MnO_2 is present; this behaviour is similar to that observed for the C peaks assigned to the oxygen functional groups. The strong oxidising properties of this oxide may be responsible for the changes that take place at the surface level of the particles, where this technique is useful. More pronounced differences are shown in the spectrum of O 1s (Fig. 2c), due to the MnO_2 content. The spectrum can be fitted to at least three components, with binding energies 528.7, 530.5 and 532.3 eV assigned to Mn-O, C-OH and C-O (or H-O-H), respectively. Finally, the two peaks in the Mn 2p spectrum ($2p_{3/2}$ and $2p_{1/2}$) (Fig. 2d) are relatively symmetric binding energies of 641.1 and 652.6 eV, which are consistent with Mn^{4+} [47].

Figure 2

Table 1. Contributions of the four components used in the fitting of the C 1s photoemission peak (in %)

Sample	C-C	C-O	C=O	O-C=O
BE (eV)	283.6	285.1	286.5	287.9
AC/S@gr	75.6	16.2	5.4	2.5
AC/MnO_2/S@gr	71.3	17.2	6.8	4.7
AC/MnO_2/S@ht	66.0	20.1	8.0	5.9

SEM images of the composites and their components are shown in Fig. 3. MnO_2 has a microsphere-shaped morphology, with a variable diameter ranging from 4–10 µm (see Fig. 3a). The microspheres are formed by agglomerates of submicronic nanorods of nanometric thickness. A fluffy type of morphology is adopted by the activated carbon (Fig. 3b). The macroparticles are agglomerates of smaller particles, as shown by the high specific surface discussed below. The sulphur forms micrometric particles of variable size and shape, a typical morphology for commercial S. Two observations can be made for the SEM images of the composites with AC/MnO_2: the first is the spherical morphology loss of the γ-MnO_2 phase and the more homogeneous distribution of the components in the $AC/MnO_2/S$@gr composite (Fig. 3c), while the second is the presence of MnO_2 microspheres and sponge-like particles of AC in the $AC/MnO_2/S$@ht composite, and the more heterogenous distribution of the components as a result. In the image of this composite (Fig. 3d), the γ-MnO_2 phase is clearly identified. Therefore the absence of peaks belonging to this phase in the XRD pattern is due to its low content in the composite. Thus, its poor crystallinity and low content appear to be the reasons for the apparent disagreement between the two characterisation techniques. The energy dispersive spectroscopy (EDS) of the elemental maps of C, O, Mn and S is shown in Figs. 3e-f. The grinding process clearly destroys the MnO_2 microspheres, and the composite exhibits a more homogeneous distribution of elements compared with that of the composite prepared under hydrothermal conditions. In this composite, the microsphere particles of MnO_2 are clearly localised and the sulphur is homogeneously distributed.

Figure 3

The sulphur content was determined from TG measurements recorded in a dynamic N_2 atmosphere (Fig S2). The sublimation of sulphur occurs in the range 180°C–360ºC for the composites with MnO_2, and in a somewhat wider range of up to 420ºC for the composite without MnO_2. In this temperature range, both the oxide and the AC matrix also lose a small amount of weight; these losses can be attributed to water and the decomposition of the containing oxygen-related functional groups, respectively (see Fig. 2a). After correcting for these weight losses, the S content calculated for the MnO_2-containing composites was 58%, and a somewhat higher value of 61% was calculated for the composite without MnO_2.

The N_2 adsorption-desorption isotherms of AC, MnO_2 and the composites are shown in Fig. 4. According to the BDDT classification, the shape adsorption of AC is type I (associated with microporous systems) and type IV at relative pressures of above 0.6. Moreover, the presence of a mesoporous system is revealed by the hysteresis loop in the desorption curve [48], which allows the use a of hierarchica0l porous system terminology for our carbon. The adsorption isotherm for MnO_2 is type II, which is typical of non-porous solids, and the small hysteresis loop at high pressure is of little significance. The composites also show type II isotherms, but with a drastic decrease in the adsorbed volume of N_2 compared to that of pristine carbon and, to a lesser extent, that of the oxide. BET surface and pore volume values are shown in Table 2. The pore size distribution evaluated using the DFT method confirms the micro-mesoporous texture of the pristine carbon (Fig. S3). The average micropore size is calculated as being between 0.7 and 1.9 nm, and wide, weak peaks appear at 3.7 and 6.5 nm, which are values in the mesopore range. The high value for the specific surface for carbon, 615 $m^2\ g^{-1}$, is due mainly to its microporosity. The specific surface of γ-MnO_2 was notably lower, at only 40 $m^2\ g^{-1}$, which is consistent with its non-porous nature. The decrease was even greater for the three composites. These values are within the limits of accuracy of the adsorption measurements, and the origin is the coating of the matrix particles by S, a material with very small BET surface values [49].

Figure 4

Table 2. Values of specific surface area and pore volume for the AC, MnO_2 and composites

Sample	S_{BET} ($m^2\ g^{-1}$)	V_{pore} ($cm^3\ g^{-1}$)	V_{micro} ($cm^3\ g^{-1}$)
AC	615	0.38	0.16
MnO_2	40	0.19	0.005
AC/S@gr	2	0.01	0.0007
AC/MnO_2/S@gr	5	0.04	0.001
AC/MnO_2/S@ht	5	0.03	0.0009

To evaluate the electrochemical properties of the composites, coin cells were assembled with composite acting as the cathode and Li metal as the anode. The galvanostatic discharge/charge curves recorded at a rate of 0.1 C (Fig. 5a-c) show two typical discharge plateaus at around 2.3 and 2.0 V for the three composites [50]. In the first plateau, the S_8 ring is opened and high long chain polysulphides are formed via the reaction: $2\ Li + nS + 2\ e^{-} \rightarrow Li_2S_n + S\ (4 \leq n \leq 8)$. In the second plateau, the breakdown of the S-S bonds continues, and the chains of the polysulphides become shorter until they form Li_2S, the most reduced form, via the reaction $Li_2S_n + 2(n-1)\ Li^{+} + 2(n-1)\ e^{-} \rightarrow nLi_2S\ (n < 4)$. On charging the cell, strong polarisation takes place, which is derived from changes in the inner resistance of the cell caused by the reaction products. The two plateaus are perceptible, but are less differentiated due to the observed polarisation, and particularly for the AC/S@gr composite. The first plateau located at approximately 2.2 V is caused by the oxidation of Li_2S to polysulphides, which continue to oxidise to S at the higher potential centred at approximately 2.3 V. The shape of the curves therefore reveals the reversibility of the electrochemical reactions undergone by S. On further cycling, no significant changes in the profile shape were detected. It its worth nothing that the polarisation between the discharge and charge curves for the three composites shows rather similar effects for AC/MnO_2/S@gr and AC/MnO_2/S@ht, and is clearly higher for the AC/S@gr composite. This can be detected more clearly in the CV curves (Fig. S4), since in addition to exhibiting the peaks typical of the plateaus described above, the polarisation between the peaks of reduction and between these and the oxidation peaks is clearly greater for the AC/S composite than for the MnO_2-based composites.

Figure 5

The discharge capacity values delivered by the three composites are shown in Fig. 5d as a function of the number of cycles at a rate of 0.1 C. To facilitate the comparison, some selected values are summarised in Table 3. The initial discharge of the AC/S@gr composite, 692 mAh g^{-1}, is notably lower than that of the composites with MnO_2. The values for these MnO_2-based composites are rather similar: 926 and 874 mAh g^{-1} for the AC/MnO_2/S@gr and AC/MnO_2/S@ht, respectively. On cycling, a decrease in the specific capacity was shown (this was more pronounced in the first cycles, in which the cell is activated). After 100 cycles, the specific capacities delivered by the AC/S@gr, AC/MnO_2/S@gr and AC/MnO_2/S@ht composites were 300, 541 and 555 mAh g^{-1}, respectively. In terms of capacity loss, the calculated values were 0.56%, 0.41% and 0.36% per charge/discharge cycle. Lower differences were observed in the values of coulombic efficiency for the three composites, which varied between 98% and 100 % after the first few cycles. It is worth noting the differences between the discharge capacity values obtained in the AC/S@gr composite and those reported in [42], which used the same carbon matrix but with S deposited via the disproportion reaction of $Na_2S_2O_3$ in an acid medium. After 100 cycles, the capacity delivered by this cell was higher (600 mAh g^{-1} at a rate of 0.06 C). This improved performance is attributed to the deposition S method, and is consistent with other reports [51,52], in which methods for in situ S deposition, such as the dissolution of S in CS_2 or thiosulphate in an acid medium, give better performance than those which use commercial S followed by grinding or melt diffusion.

Table 3. Discharge capacity values delivered by the composites at different cycles (mAh g^{-1}) for a rate of 0.1 C

Composite/cycle	1st	10th	50th	100th
AC/S@gr	692	499	353	300
AC/MnO_2/S@gr	926	710	611	541
AC/MnO_2/S@ht	874	702	592	555

The long-term cycling stability of the electrode was also tested at higher rates of 0.5 and 1 C after being activated at C/16 for two cycles. The results are shown in Figs. 5e and 5f, and are presented in Table 4. After this activation and the subsequent drop in specific capacity, the capacity delivered by the AC/S@gr, AC/MnO_2/S@gr and AC/MnO_2/S@ht composites at the third cycle was 460, 507 and 522 mAh g^{-1} at 0.5 C, and 159, 493 and 489 mAh g^{-1} at 1 C, respectively. After 100 cycles, the discharge capacities of the AC/S@gr, AC/MnO_2/S@gr and AC/MnO_2/S@ht composites decreased to 349, 401 and 464 mAh g^{-1} at 0.5 C and to 120, 295 and 300 mAh g^{-1} at a rate of 1C. These results confirm the beneficial role played by MnO_2 in the electrochemical reaction between Li and S, as evidenced by a clear increase in the discharge capacity values observed at lower current densities and a less pronounced increase in the coulombic efficiency values. Moreover, there is a persistent (although limited) influence from the composite preparation method, in this case grinding or hydrothermal procedures.

Table 4. Discharge capacity values delivered by the composites at different cycles (mAh g^{-1}) at rates of 0.5 C and 1 C

Composite	Cycle	3rd		10th		50th		100th	
	Rate	0.5 C	1 C	0.5 C	1 C	0.5 C	1 C	0.5 C	1 C
AC/S@gr		460	159	327	115	399	119	349	120
AC/MnO_2/S@gr		522	493	529	460	508	345	464	296
AC/MnO_2/S@ht		507	489	529	468	479	363	401	300

EIS measurements were also used to compare the resistance between the electrodes, based on the three composites in the Li/S cells at open circuit voltage (OCV) and after cycling, in order to shed light on the reason for the improved electrochemical performance induced by the presence of MnO_2. The corresponding Nyquist plots are shown in Fig. 6a. The semicircle in the high-/medium-frequency region is assigned to the charge transfer taking place at the electrolyte/electrode interface, and the straight line in the low-frequency region is ascribed to semi-infinite diffusion (Warburg impedance). Interestingly, under OCV conditions, the charge transfer resistances of the AC/MnO_2/S@ht and AC/MnO_2/S@gr electrodes are 540 and 610 Ω, respectively. These values are relatively similar compared with the significant increase in the value measured for the AC/S@gr composite of 790 Ω. The explanation of these results considering the electrical conductivities of AC and MnO_2 is difficult taking into account the numerous intrinsic and extrinsic factors that affect the measurement of this property. The only value of the electrical conductivity of an activated carbon from biomass found has been that reported by Barroso-Bojeat et al., 54.3 S m^{-1} [53]. The available data of the conductivity of MnO_2 are more abundant although they are serious disprepancies from values oscillate from 200 S m^{-1} [54], 0.06 S m^{-1} [55] and 5.10^{-4} S m^{-1} [56]. Even some authors describe an increase in the conductivity for MnO_2/CB (carbon black) composites by increasing the oxide content [57]. Unfortunately the measurement of the electrical properties of our composites is beyond our reach, hence this property raises doubts as to the origin of the observed behavior. After three cycles, the interfacial transport resistance of the three electrodes decreased; this is commonly observed [58-61] behaviour which is associated with an improvement in the interfacial contact between the S species and conductive components, due to the transformation of S to soluble polysulphides. The approximate values of the resistances for the AC/MnO_2/S@ht, AC/MnO_2/S@gr and AC/S@gr electrodes were 115, 130 and 300 Ω, respectively. Clearly, the presence of MnO_2 in the electrode gave rise to a decrease in the charge transfer resistance, which becomes more pronounced when cycling the cell. In later cycles, the decrease slows down. Considering that MnO_2 is virtually electrochemically inactive within the voltage window used [62] (1.8–2.7 V), the improvement in cell performance must be related to its ability to constrain the dissolution of the polysulphides, thus hindering their diffusion between the cathode and anode [63]. The exposed S surface would be passivated by polysulfides forming a passivation layer the thickness of which would increase in parallel to the amount of polysulfides dissolved in the electrolyte. The absorption capacity of the oxide towards these species would hinder the growth of the passivation layer a a decrease in the resistance as a result. This inherent property of MnO_2 would explain the irrelevance of the composite preparation method (grinding and hydrothermal treatment) despite the significant differences induced in the particle morphology. This may also be the reason for the difficulty in correlating the crystalline structure, the particle morphology and the content of MnO_2 with the observed performance of the Li/S cell [23-35].

Figure 6

Table 5 presents some selected properties of Li/S batteries made from C/MnO_2/S composites recently reported in the literature, in order to carry out a comparison with our results. Since our aim is to examine the role played by MnO_2 in the performance of the cell, we have chosen articles that include electrochemical data for cells made from C/S and C/MnO_2/S composites, in order to identify with more accuracy the real improvement in the battery performance caused by the presence of MnO_2. Other features taken into consideration were as follows: (i) in order to investigate the cycling properties, the number of cycles was extended to 100; (ii) the amount of MnO_2 and S in the composites; (iii) a brief description of the experimental conditions used for the C preparation together with its source, the S impregnation method and the crystalline phase and morphology of MnO_2. The oxide content of our composites has an average value, while the S content of around 60% is somewhat lower than most of the values in the table, but is high enough for practical applications. The first observation made was the difficulty in establishing a clear correlation between the experimental conditions and the electrochemical response of the electrode. In most of the references, resorcinol-formaldehyde was chosen as the carbon source, and silica is used as a template to tailor the particle morphology and the melt-diffusion method used for S impregnation. Despite these similarities, there are significant differences between the capacity values in the initial cycles and after 100 cycles, which makes it difficult to compare the real improvement produced by the oxide. To overcome this issue, we include a column containing the ratio between the capacity values delivered by the composite, with and without oxide, at the 100th cycle. These values better define the contribution of the oxide to the improvement in battery performance, and make a comparison easier and more reliable. According to these values, the beneficial effect of our MnO_2 on the performance of the cell is among the best of those included in the table, particularly at low to moderate values of current (0.1 to 0.2 C). Even at a higher current (1 C) the values of approximately 2.5 obtained from Table 4 are still remarkable.

Table 5. Selected properties of Li/S cells made from different carbon/MnO_2 composites

Carbon, sulphur and MnO_2 components	Composite	C_i (a)	C_{100} (a)	MnO_2 (%)	Rate (C)	S (%)	Ratio C_{100} (b)	Ref.
Activated carbon from olive stones S (gr) γ-MnO_2 nanorods	AC/S AC/MnO_2/S@gr AC/MnO_2/S @ht	693 926 874	300 541 555	20	0.1	62 59 60	 1.85 1.80	This study
C nanofibers (RF), SiO_2(t) S (md) α-MnO_2 nanowires	C/S MnO_2/C/S	1216 1147	400 900	17	0.2 0.2	71 71	 2.25	[28]
N-doped C nanospheres (RF;PPy), SiO_2 (t) S (md) δ-MnO_2 nanosheets.	C/S MnO_2/C /S	1216 1283	1000 1125	27	0.2	69	 1.12	[29]
RF-derived C, SiO_2 (t) S (md) δ-MnO_2 nanocubes	C/S MnO_2/C/S	875 1042	100 500	37	1	68	 5.0	[30]
GO, CNT S (md) δ-MnO_2	C/S MnO_2/C/S	980 1100	532 825	11	0.2	78	 1.55	[31]
CMK-3 S (md) MnO_2	C/S MnO_2/C/S	950 1050	350 600	7	0.1	79 73	 1.71	[32]

N-C spheres S (CdS) MnO_2	S/C MnO_2/C/S	725 1150	300 400	11	0.1	71 60	1.33	[33]
N-doped carbon (melamine,RF), SiO_2(t) S (md) δ-MnO_2 nanosheets	C/S MnO_2/C/S	1176 1050	825 976	22	0.5	70 68	1.18	[34]
Mesoporous carbon (RF) SiO_2 (t) S (md) δ-MnO_2 nanospheres	S/C MnO_2/C/S	800 1142	225 850	26	0.5	84 58	3.77	[35]

[(a)] mAh g^{-1}; [(b)] Ratio = $C_{100\ (C/MnO2/S)}$ / $C_{100\ (C/S)}$
RF: resorcinol-formaldehyde; t: template; gr: grinding; md: melt-diffusion

The rate capability of the composites was further examined at rates of current of between 0.1 and 1 C (see Fig. 6b). The similar electrochemical behavior already described for the AC/MnO_2/S@gr and AC/MnO_2/S@ht composites was also observed in these tests; hence, we include in the figure the data for a composite prepared using a hydrothermal treatment, AC/MnO_2/S@ht. As expected, the discharge capacity becomes lower as the current rate increases. However, a more pronounced decrease in the discharge capacity was observed at 0.1 C, particularly in the first three cycles, from 1190 to 825 mAh g^{-1} for the AC/MnO_2/S@ht composite and somewhat less, from 710 to 650 mAh g^{-1}, for the AC/S@gr composite. At other rates, the delivered capacity tended to stabilise. The average values measured were about 650, 600, 560, 530 and 500 mAh g^{-1} for rates of 0.2, 0.5, 0.8 and 1 C, respectively, for the AC/MnO_2/S@ht composite, and 420, 300, 210 and 170 mAh g^{-1} for rates of 0.2, 0.5, 0.8 and 1 C, respectively, for the AC/S@gr composite. When the current was changed back to 0.1 C, the AC/MnO_2/S@ht and AC/S@gr composites almost recovered their original capacities of 620 and 470 mAh g^{-1}, respectively. Again, the beneficial role played by MnO_2 is obvious.

The beneficial contribution of MnO_2 is mainly ascribed to its high oxidising power, which gives it the ability to oxidise polysulphides, and the in situ formation of thiosulphate/polythionate, as suggested by Liang et al. [63] and further investigated by Ni et al. [64]. Moreover, the nanometric size of the particles and the significant surface value enhance the interaction between MnO_2 and the polysulphides. This hinders the diffusion of polysulphides in the electrolyte and the loss of S, and moderates the shuttle effect as a result. Experimental evidence on this hypothesis was obtained from two complementary measures (i) study of the absorption properties of carbon and oxide towards polysulfides and (ii) the analysis of the S distribution in the composites after cell cycling. The adsorption properties of the AC and MnO_2 towards polysulfides, prepared according to previously reported literature [65], is shown in Fig. S5. The intensity of the yellow-brown color decreases more sharply in contact with MnO_2 than with the carbon matrix. The intensity of the brown color of polysulfide disappeared upon contact with the carbon matrix. The Vis/UV spectrum gives further support to this observation since the intensity of the peak at 450 nm, responsible of the yellow-brown color of polysulfide, suffers a slight decrease in contact with carbon. By contrast, when in contact with the pure oxide or mixed with carbon, the peak hardly becomes discernable. These data confirm the better absorption ability to polysulfides of MnO_2 and the improved performance of the cell as a result.

Post-mortem stadies of the electrodes were carrie out in the charge state on cycling the cell up to 100 cycles. After dismantling the cells, washing the electrodes with electrolyte solvents to remove electrolyte salt and drying, the surface morphology and composition were analysed by SEM-EDS. The SEM images shown in Fig. S6 a, b reveal that the presence of MnO_2 causes a greater compaction of the electrode and consequently a better connectivity between the deposit particles, thus decreasing the electrode resistance consistent with EIS data (Fig. 6a). The extent of S agglomeration with cycling was deduced from the EDS data of the deposits. Before cycling, the mapping of deposits with and without MnO_2 shows a distribution of the S throughout their surface but with certain areas where its concentration becomes higher, Fig. S7 a, b. The main effect of cycling is a decrease in the intensity of the S signal, but in the AC/S composite there are still area of high S concentration Fig. S7a). By contrast, a more homogeneous distribution of S is observed when MnO_2 is present (Fig. 7S b), thus indicating that the extent of S agglomeration is greatly reduced. The S content directly obtained from the spectra (without introducing any correction due to the signals of other elements present, O, Al, F ... and without following a determined schedule to obtain accurate composition values) is shown in Table S1. As expected, The S content of AC/S and AC/MnO_2/S@ht composites is quite similar (like AC/MnO_2/S @gr composite not shown). The S percentage, somewhat higher than 20%, is far from that calculated from TG data the reason of which the reason is that by not performing an exhaustive treatment to quantify the technique, the composition values are qualitative but valid to clarify the role played by MnO_2. After cycling a S loss is observed caused the "shuttle effect". This loss is specially pronounced for the AC/S composite being another proof of the mitigating bahavior of MnO_2 on the shuttle effect. These results confirm that the cells with MnO_2 improve the utilization of S and display better cycling behaviour and delerever higher capacities.

4. Conclusions

In summary, the use of γ-MnO_2 nanorods synthesised using a hydrothermal method is a good candidate for improving the capacity and cycling properties of carbon/sulfur composites in Li/S batteries. The advantage of these composites in comparison with others reported in the literature is the use of simple and inexpensive procedures for the preparation of the components. A biomass-derived microporous carbon was used, mixed with commercial S either by wet grinding or magnetic stirring. γ-MnO_2 was incorporated either by in situ growth under hydrothermal conditions or by grinding. Compared to the AC/S composite, the capacity of the AC/MnO_2/S composite increases by more than 80% at 0.1 C and around 145% at 1 C, and these values are affected very little by the preparation method. The improved performance is ascribed to the ability of the polar MnO_2 to trap and confine the generated polysulphides via a synergistic combination of its strong oxidising properties and the nanorod morphology, revealed by the relatively high specific surface area for this type of compound. The observed improvement is comparable with and even superior to those reported for other forms of carbon preparation and S impregnation, which are more complex and expensive.

Acknowledgements

This work was supported by the Ministerio de Economía, Industria y Competitividad [Projects MAT2014-59907-R and MAT2017-87541-R] and Junta de Andalucía [Group FQM-175].

References

[1] J.M. Tarascon, M. Armand, Issues and challenges facing rechargeable lithium batteries. Nat. 414 (2001) 359-367.

[2] A.S. Arico, P. Bruce, B. Scrosati, J.M. Tarascon, W. van Schalkwijk, Nanostructured materials for advanced energy conversion and storage devices. Nat. Mater., 4 (2005) 366–377.

[3] J.B. Goodenough, Y. Kim, Challenges for Rechargeable Li Batteries. Chem. Mater. 22 (2010) 587-603.

[4] E.J. Cairns, P. Albertus, Batteries for Electric and Hybrid-Electric Vehicles. In Annual Review of Chemical and Biomolecular Engineering; Prausnitz, J. M., Doherty, M. F., Segalman, M. A., Eds.; Annual Reviews: Palo Alto, 1 (2010) 299−320.

[5] Y. Yang, G. Zheng, Y. Cui, Nanostructured sulfur cathodes. Chem. Soc. Rev. 42 (2013) 3018-3032.

[6] A. Manthiram, Y. Fu, S.H. Chung, C. Zu, Y.S. Su, Rechargeable Lithium–Sulfur Batteries. Chem Rev. 114 (2014) 11751-11787.

[7] R. Xu, J. Lu, K. Amine Progress in mechanistic understanding and characterization techniques of Li-S batteries. Adv. Energy Mater. 5 (2015) 1500408.

[8] R. Fang, S. Zhao, Z. Sun, D.W. Wang, H.M. Cheng, F. Li. More Reliable Lithium-Sulfur Batteries: Status, Solutions and Prospects. Adv. Mater. 29 (2017) 1606823.

[9] Y. Yang, G. Zheng, Y. Cui. Nanostructured Sulfur Cathodes. Chem. Soc. Rev. 42 (2013) 3018-3032.

[10] Z. Zeng, X. Liu, Sulfur Immobilization by "Chemical Anchor" to Suppress the Diffusion of Polysulfides in Lithium–Sulfur Batteries. Adv. Mater. Interface 5 (2018) 1701274.

[11] Y.X. Yin, S. Xin, Y.G. Guo, L.J. Wan, Lithium-sulfur batteries: electrochemistry, materials, and prospects. Angew. Chem. Int. Ed. 52 (2013) 13186-13200.

[12] D.W. Wang, C. Zeng, G.M. Zhou, L.C. Yin, F. Li, H.M. Cheng, I.R. Gentle, G.Q.M. Lu, Carbon–Sulfur Composites for Li–S Batteries: Status and Prospects. J. Mater. Chem. A 1 (2013) 9382–9394.

[13] F. Xu, Z. Tang, S. Huang, L. Chen, Y. Liang,W. Mai, H. Zhon, R. Fu, D. Wu Facile synthesis of ultrahigh-surface-area hollow carbon nanospheres for enhanced adsorption and energy storage. Nat. Commun. 6 (2015) 7221.

[14] X. Liang, C.Y. Kwok, F. Lodi- Marzano, Q. Pang, M. Cuisinier, H. Huang, C.J. Hart, D. Houtarde, K. Kaup, H. Sommer, T. Brezesinski, J. Janek, L.F. Nazar, Lithium- Sulfur Batteries: Tuning Transition Metal Oxide–Sulfur Interactions for Long Life Lithium Sulfur Batteries: The "Goldilocks" Principle. Adv. Energy Mater. 6 (2016) 1501636.

[15] Z. W. Seh, W. Li, J.J. Cha1, G. Zheng, Y. Yang, M.T. McDowell, P.C. Hsu, Y. Cui, Sulphur–TiO_2 yolk–shell nanoarchitecture with internal void space for long-cycle lithium–sulphur batteries. Nat. Commun. 4 (2013) 1331.

[16] Q. Pang, D. Kundu, M. Cuisinier, L.F. Nazar, Surface-enhanced redox chemistry of polysulphides on a metallic and polar host for lithium-sulphur batteries. Nat. Commun. 5 (2014) 4759.

[17] X. Liang, L.F. Nazar, In-situ Reactive Assembly of Scalable Core-Shell Sulfur-MnO_2 Composite Cathodes. ACS Nano 10 (2016) 4192–4198.

[18] L. Ni, Z. Wu, G. Zhao, C. Sun, C. Zhou, X.X. Gong, G. Diao, Core–Shell Structure and Interaction Mechanism of γ-MnO_2 Coated Sulfur for Improved Lithium-Sulfur Batteries. Small 13 (2017) 1603466.

[19] B. Ding, G. Xu, L. Shen, P. Nie, P. Hu, H. Doua, X. Zhang, Fabrication of a sandwich structured electrode for highper formance lithium–sulfur batteries. J. Mater. Chem. A 1 (2013) 14280-14285.

[20] H. Wang, S. Li, D. Li, Z. Chen, H.K. Liu, Z. Gu, TiO_2 coated three-dimensional hierarchically ordered porous sulfur electrode for the lithium/sulfur rechargeable batteries. Energy 75 (2014) 595-602.

[21] G. Zhou, Y. Zhao, C. Zu, A. Manthiram, Free-standing TiO_2 nanowire-embedded graphene hybrid membrane for advanced Li/dissolved polysulfide batteries. Nano Energy 12 (2015) 240-249.

[22] N. Moreno, A. Caballero, J. Morales, E. Rodríguez-Castellón, Improved performance of electrodes based on carbonized olive stones/S composites by impregnating with mesoporous TiO_2 for advanced Li-S batteries. J. Power Sources, 313 (2016) 21-29.

[23] C.M. Julien, A. Mauger, Nanostructured MnO_2 as Electrode Materials for Energy Storage. Nanomaterials 7 (2017) 396.

[24] J. Guo, X. Zhang, X. Du, F. Zhang, A Mn_3O_4 Nano-Wall Array Based Binder-free Cathode for High Performance Lithium–Sulfur Batteries. J. Mater. Chem. A 5 (2017) 6447-6454.

[25] X. Huang, K. Shi, J. Yang, G. Mao, J. Chen, MnO_2-GO double-shelled sulfur (S@MnO_2@GO) as a cathode for Li-S batteries with improved rate capability and cyclic performance. J. Power Sources 356 (2017) 72-79.

[26] X. Zhao, G. Wang, G. Zhai, H. Wang, Facile Assembly of 3D Porous Reduced Graphene Oxide/Ultrathin MnO_2 Nanosheets-S Aerogels as Efficient Polysulfide Adsorption Sites for High-Performance Lithium–Sulfur Batteries. Chem Eur. J. 23 (2017) 1-10.

[27] L. Ni, G. Zhao, Y. Wang, Z. Wu, W. Wang, Y. Liao, G. Yang, G. Diao, Coaxial Carbon/MnO_2 Hollow Nanofibers as Sulfur Hosts for High-Performance Lithium-Sulfur Batteries. Chem. Asian J. 12 (2017) 3128-3134.

[28] Z. Li, J. Zhang, X.W.D. Lou, Hollow Carbon Nanofibers Filled with MnO_2 Nanosheets as Efficient Sulfur Hosts for Lithium-Sulfur Batteries, Angew. Chemie Int. Ed. 54 (2015) 12886–12890.

[29] M. Chen, Q. Lu, S. Jiang, C. Huang, X. Wang, B. Wu, K. Xiang, Y. Wu, MnO_2 nanosheets grown on the internal/external surface of N-doped hollow porous carbon nanospheres as the sulfur host of advanced lithium-sulfur batteries, Chem. Eng. J. 335 (2018) 831–842.

[30] S. Rehman, T. Tang, Z. Ali, X. Huang, Y. Hou, Integrated Design of MnO_2@Carbon Hollow Nanoboxes to Synergistically Encapsulate Polysulfides for Empowering Lithium Sulfur Batteries, Small 13 (2017) 1–8.

[31] Y. Li, D. Ye, W. Liu, B. Shi, R. Guo, H. Zhao, H. Pei, J. Xu, J. Xie, A MnO_2/Graphene Oxide/Multi-Walled Carbon Nanotubes-Sulfur Composite with Dual-Efficient Polysulfide Adsorption for Improving Lithium-Sulfur Batteries, ACS Appl. Mater. Interfaces 8 (2016) 28566–28573.

[32] J. Liu, C. Wang, B. Liu, X. Ke, L. Liu, Z. Shi, H. Zhang, Z. Guo, Rational synthesis of MnO_2@CMK/S composite as cathode materials for lithium–sulfur batteries, Mater. Lett. 195 (2017) 236–239.

[33] J. Liu, J. Shen, Z. Liu, R. Hu, J. Liu, M. Zhu, Nanoconfined Oxidation Synthesis of N-Doped Carbon Hollow Spheres and MnO_2 Encapsulated Sulfur Cathode for Superior Li-S Batteries, Chem. Eur. J. 24 (2018) 4573-4582.

[34] X. Zhang, H. Yang, J. Guo, S. Zhao, S. Gong, X. Du, F. Zhang, Nitrogen-doped hollow porous carbon nanospheres coated with MnO_2 nanosheets as excellent sulfur hosts for Li–S batteries. Nanotechnology 28 (2017) 475401.

[35] L. Ni, G. Zhao, G. Yang, G. Niu, M. Chen, G. Diao, Dual Core–Shell-Structured S@C@MnO_2 Nanocomposite for Highly Stable Lithium–Sulfur Batteries. ACS Appl. Mater. Interfaces 9 (2017) 34793–34803.

[36] M. Danish, T. Ahmad, A review on utilization of wood biomass as a sustainable precursor for activated carbon production and application. Renew. Sust. Energ. Rev. 87 (2018) 1–21.

[37] Z. Gao, Y. Zhang, N. Song, X. Li, Biomass-derived renewable carbon materials for electrochemical energy storage. Mater. Res. Lett. 5 (2017) 69-88.

[38] J. Li, F. Qin, L. Zhang, K. Zhang, Q. Li, Y. Lai, Z. Zhang, J. Fang, Mesoporous carbon from biomass: one-pot synthesis and application for Li-S batteries. J. Mater. Chem. A 2 (2014) 13916-13922.

[39] J. Guo, J. Zhang, F. Jiang, S. Zhao, Q. Su, G. Du, Microporous carbon nanosheets derived from corncobs for lithium-sulfur batteries. Electrochim. Acta 176 (2015) 853-860.

[40] Z.J. Sun, S.J. Wang, L.L. Yan, M. Xiao, D.M. Han, Y.Z. Meng, Mesoporous carbon materials prepared from litchi shell as sulfur encapsulator for lithium-sulfur battery application. J. Power Sources 324 (2016) 547-555.

[41] M. Raja, N. Angulakshmi, A. M. Stephan, Sisal-derived activated carbons for cost-effective lithium-sulfur batteries. RSC Adv. 6 (2016) 13772-13779.

[42] C. Hernández-Rentero, R. Córdoba, N. Moreno, A. Caballero, J. Morales, M. Olivares-Marín, V. Gómez-Serrano, Low-Cost Disordered Carbons for Li/S Batteries: A High-Performance Carbon with Dual Porosity Derived from Cherry Pits. Nano Res. 11 (2018) 89-100.

[43] N. Moreno, A. Caballero, L. Hernan, J. Morales, Lithium-sulfur batteries with activated carbons derived from olive stones. Carbon 70 (2014) 241-248.

[44] X. Gu, J. Yue, L. Li, H. Xue, J. Yang, X. Zhao, General Synthesis of MnOx (MnO_2, Mn_2O_3, Mn_3O_4, MnO) Hierarchical Microspheres as Lithium-ion Battery Anodes. Electrochim. Acta 184 (2015) 250–256.

[45] J.C. Arrebola, A. Caballero, L. Hernán, J. Morales, M. Olivares-Marín, V. Gómez-Serrano, Improving the performance of biomass-derived carbons in Li-ion batteries by controlling the lithium insertion process. J. Electrochem. Soc. 157 (2010) A791-A797.

[46] O. Vargas, A. Caballero, J. Morales, E. Rodríguez-Castellón, Contribution to the Understanding of Capacity Fading in Graphene Nanosheets Acting as an Anode in Full Li-Ion Batteries. ACS Appl. Mater. Interfaces 6 (2014) 3290−3298.

[47] J.F. Moulder, W.F. Stickle, P.E. Sool, K.D. Bomber, *Handbook of X-ray Photoelectron Spectroscopy*, Perkin-Elmer, Eden Prairie, 1992.

[48] K.S.W. Sing. Reporting Physisorption Data for Gas/Solid Systems. Pure & Appl. Chem. 57 (1985) 603-619.

[49] S.J. Chapman, Powdered elemental sulphur: oxidation rate, temperature dependence and modelling. Nutr. Cycl. Agroecosys. 47 (1996) 19-28.

[50] N. Jayaprakash, J. Shen, S.S. Moganty, A. Corona, L.A. Archer, Porous Hollow Carbon@Sulfur Composites for High- Power Lithium–Sulfur Batteries Angew. Chem. Int. Ed. 50 (2011) 5904-5908.

[51] T.A. Zegeye, M.C. Tsai, J.H. Cheng, M.H. Lin, H.M. Chen, J. Rick, W.N. Su, C.F.J. Kuo, B.J. Hwang, Controllable embedding of sulfur in high surface area nitrogen doped three dimensional reduced graphene oxide by solution drop impregnation method for high performance lithium-sulfur batteries. J. Power Sources 353 (2017) 298-311.

[52] T.G. Jeong, J. Chun, B.W. Cho, J. Lee, Y.T. Kim, Enhanced performance of sulfur infiltrated bimodal mesoporous carbon foam by chemical solution deposition as cathode materials for lithium sulfur batteries. Sci. Rep. 7 (2017) 42238.

[53] A. Barroso-Bogeat, M. Alexandre-Franco, C. Fernandez-Gonzalez, A. Macıas-García, V. Gómez-Serrano. Electrical Conductivity of Activated Carbon–Metal Oxide Nanocomposites under Compression: a Comparison Study. Phys.Chem.Chem.Phys.16 (2014) 25161-25176.

[54] P. H. Klose, Electrical Properties of Manganese Dioxide and Manganese Sexquioxide. J. Electrochem Soc. 117 (1970) 854-858.

[55] M. Moalleminejad, D.D.L. Chung Dielectric constant and electrical conductivity of carbon black as an electrically conductive additive in a manganese-dioxide electrochemical electrode, and their dependence on electrolyte permeation. Carbon, 91 (2015) 76-87.

[56] Y. Qiu, P. Xu, B. Guo, Z. Cheng, H. Fan, M. Yang, X. Yang, J. Li, Electrodeposition of manganese dioxide film on activated carbon paper and its application in supercapacitors with high rate capability. RSC Advances 4 (2014) 64187–64192.

[57] A. Gambou-Bosca, D. Belanger Chemical Mapping and Electrochemical Performance of Manganese Dioxide/Activated Carbon Based Composite Electrode for Asymmetric Electrochemical Capacitor. J. Electrochem. Soc. 162 (2015) A5115-5123.

[58] W. Qian, Q. Gao, K. Yang, W. Tian, Y. Tan, C. Yang, H. Zhang, Z. Li, L. Zhu, 3D Hierarchically Interconnected Porous Graphene Containing Sulfur for Stable High Rate Li–S Batteries. Energy Technol. 4 (2016) 625-632.

[59] F.F. Zhang, C.L. Wang, G. Huang, D.M. Yin, L.M. Wang, Enhanced electrochemical performance by a three-dimensional interconnected porous nitrogen-doped graphene/carbonized polypyrrole composite for lithium–sulfur batteries. RCS Adv. 6 (2016) 26264-26270.

[60] L. Li, G. Zhou, L. Yin, N. Koratkar, F. Li, H.M. Cheng, Stabilizing sulfur cathodes using nitrogen-doped graphene as a chemical immobilizer for Li-S batteries. Carbon 108 (2016) 120-126.

[61] R. Ummethalaa, M. Fritzschea, T. Jaumanna, J. Balacha, S. Oswalda, R. Nowakc, N. Sobczakc, I. Kabana, M.H. Rümmelia, L. Giebelera, Lightweight, free-standing 3D interconnected carbon nanotube foam as a flexible sulfur host for high performance lithium-sulfur battery cathodes. Energy Storage Mater. 10 (2018) 206-215.

[62] J. Chen, Y. Wang, X. He, S. Xu, M. Fang, X. Zhao, Y. Shang, Electrochemical properties of MnO_2 nanorods as anode materials for lithium ion batteries. Electrochim. Acta, 142 (2014) 152-156.

[63] X. Liang, C. Hart, Q. Pang, A. Garsuch, T. Weiss, L.F. Nazar, A highly efficient polysulfide mediator for lithium–sulfur batteries. Nat. Commun. 6 (2015) 5682-5687.

[64] L. Ni, Z. Wu, G. Zhao, C. Shun, C. Zhou, X. Gong, G. Diao, Core-Shell Structure and Interaction Mechanism of γ-MnO_2 Coated Sulfur for Improved Lithium-Sulfur Batteries. Small, 13 (2017) 1603466.

[65] F. Chen, L. Ma, J. Ren, X. Luo, B. Liu, X. Zhou, Sandwich-Type Nitrogen and Sulfur Codoped Graphene-Backboned Porous Carbon Coated Separator for High Performance Lithium-Sulfur Batteries. Nanomaterials, 8 (2018) 191-208.

List of figures

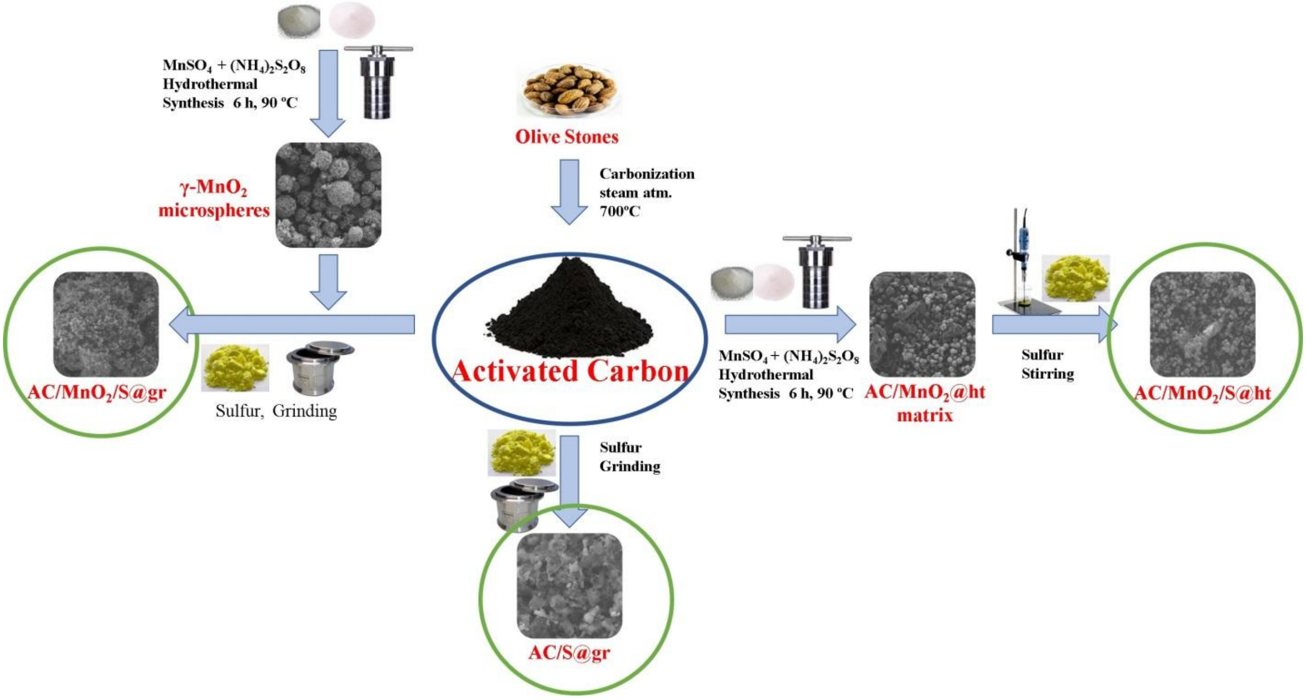
MnSO4 + (NH4)2S2O8
Hydrothermal
Synthesis 6 h, 90 °C
Olive Stones
γ-MnO2
microspheres
Carbonization
steam atm.
700ºC
Activated Carbon
AC/MnO2/S@gr
Sulfur, Grinding
MnSO4 + (NH4)2S2O8
Hydrothermal
Synthesis 6 h, 90 °C
AC/MnO2@ht
matrix
Sulfur
Stirring
AC/MnO2/S@ht
Sulfur
Grinding
AC/S@gr

Figure 1.

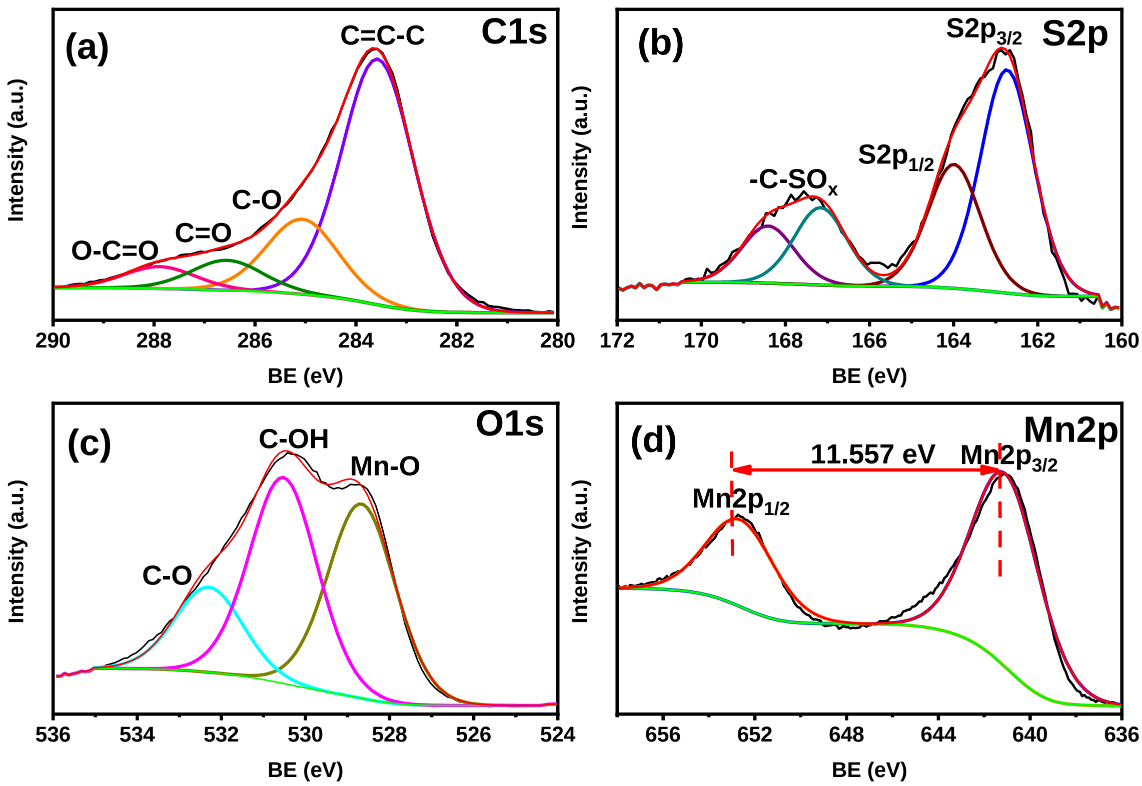
(a)
C1s
C=C-C
C-O
C=O
O-C=O
Intensity (a.u.)
BE (eV)
(b)
S2p
S2p3/2
S2p1/2
-C-SOx
Intensity (a.u.)
BE (eV)
(c)
O1s
C-OH
Mn-O
C-O
Intensity (a.u.)
BE (eV)
(d)
Mn2p
11.557 eV
Mn2p3/2
Mn2p1/2
Intensity (a.u.)
BE (eV)

Figure 2.

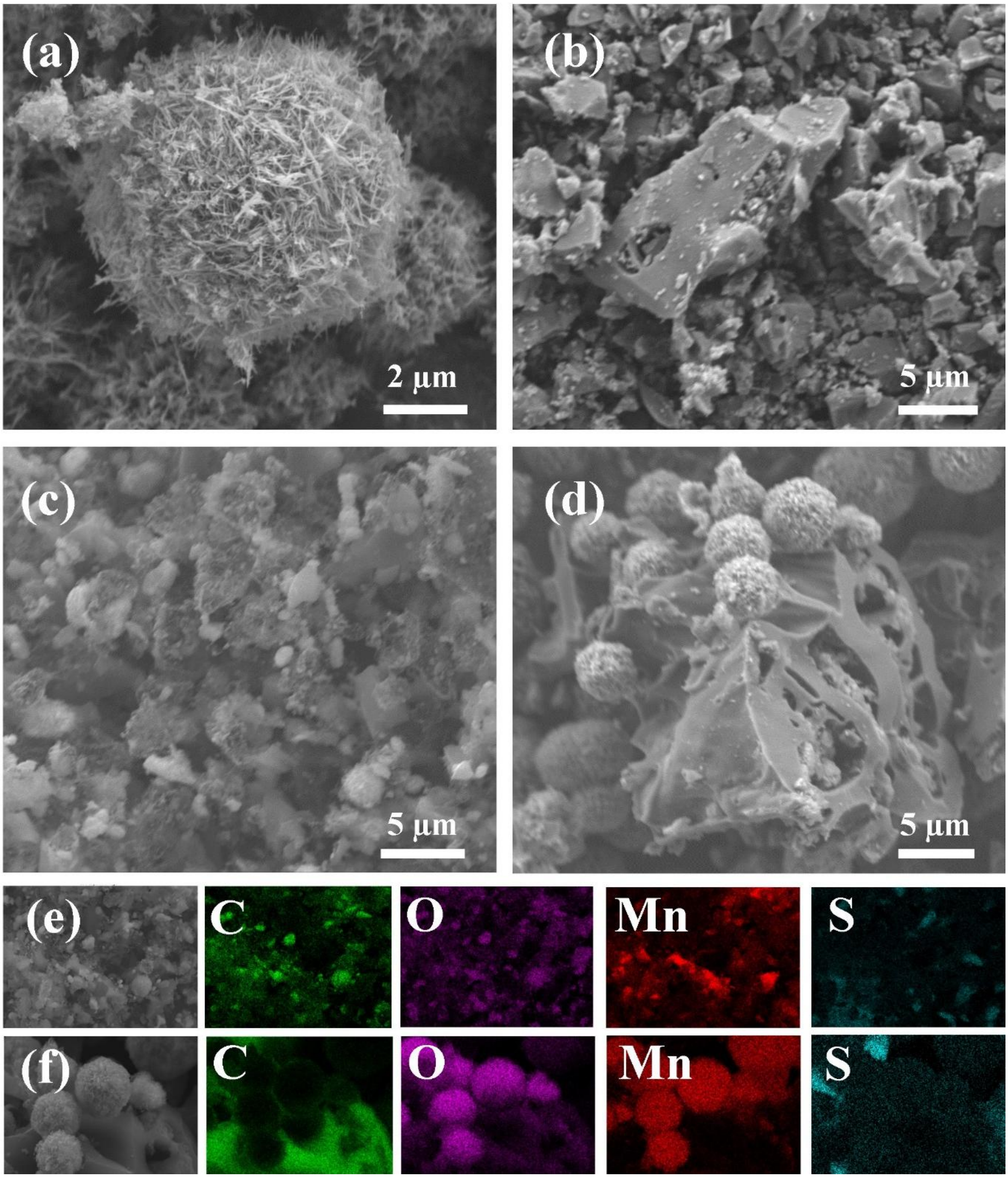

Figure 3.

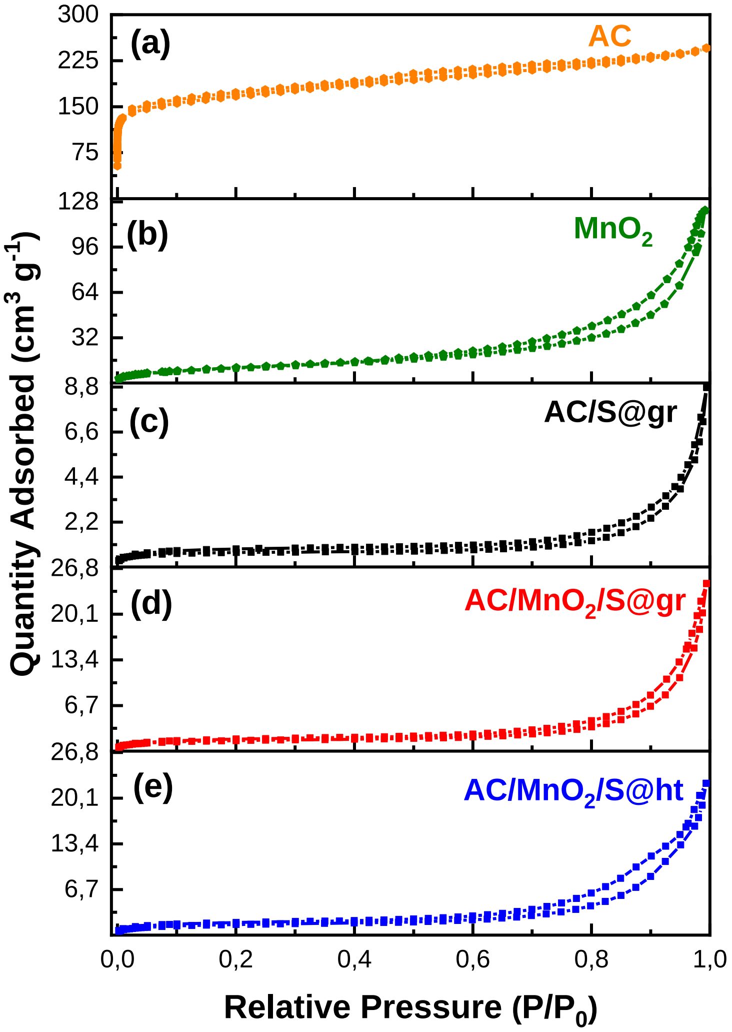
(a)
AC
(b)
MnO2
(c)
AC/S@gr
(d)
AC/MnO2/S@gr
(e)
AC/MnO2/S@ht
Quantity Adsorbed (cm3 g-1)
Relative Pressure (P/P0)
300
225
150
75
128
96
64
32
8,8
6,6
4,4
2,2
26,8
20,1
13,4
6,7
26,8
20,1
13,4
6,7
0,0
0,2
0,4
0,6
0,8
1,0

Figure 4.

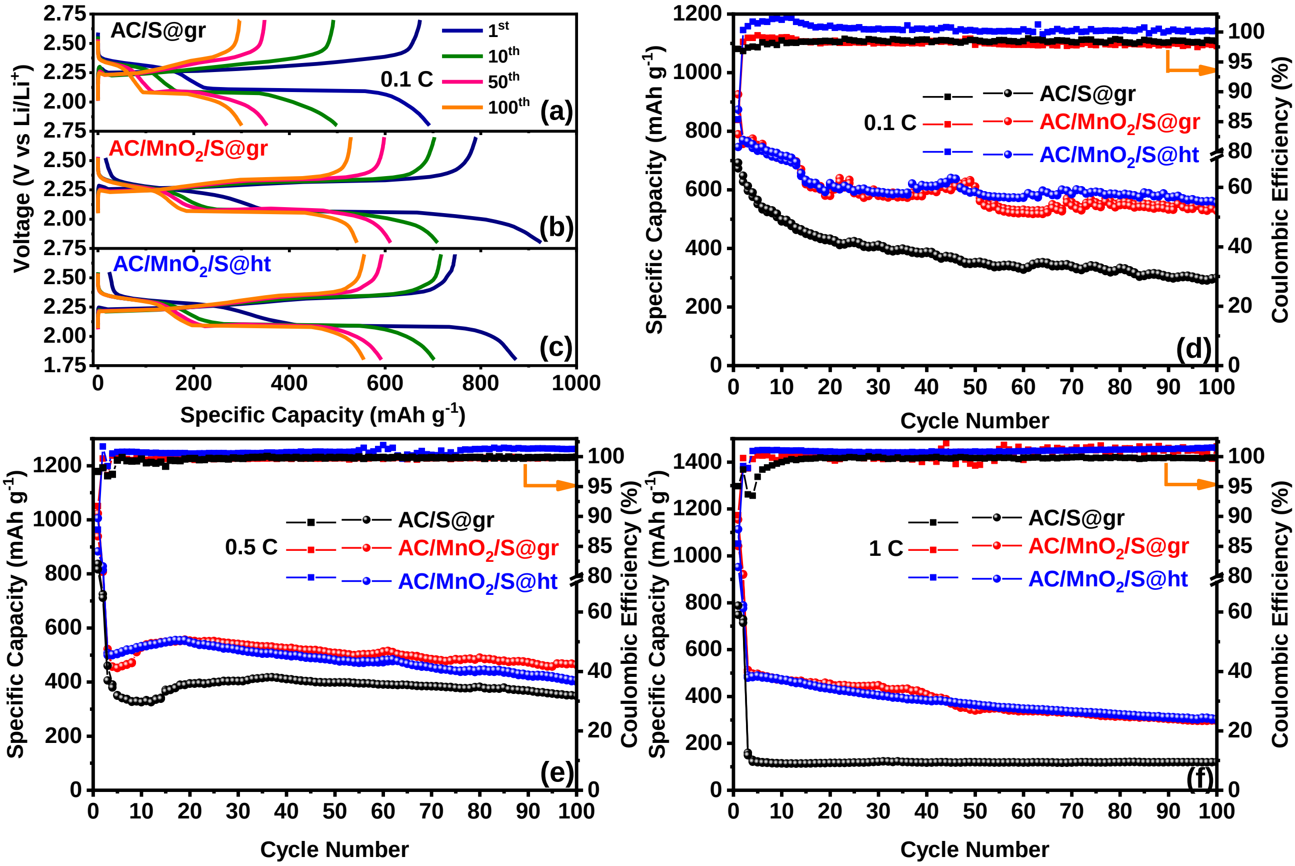
AC/S@gr
AC/MnO2/S@gr
AC/MnO2/S@ht
0.1 C
1st
10th
50th
100th
(a)
(b)
(c)
(d)
(e)
(f)
Voltage (V vs Li/Li+)
Specific Capacity (mAh g-1)
Cycle Number
Coulombic Efficiency (%)
0.5 C
1 C

Figure 5.

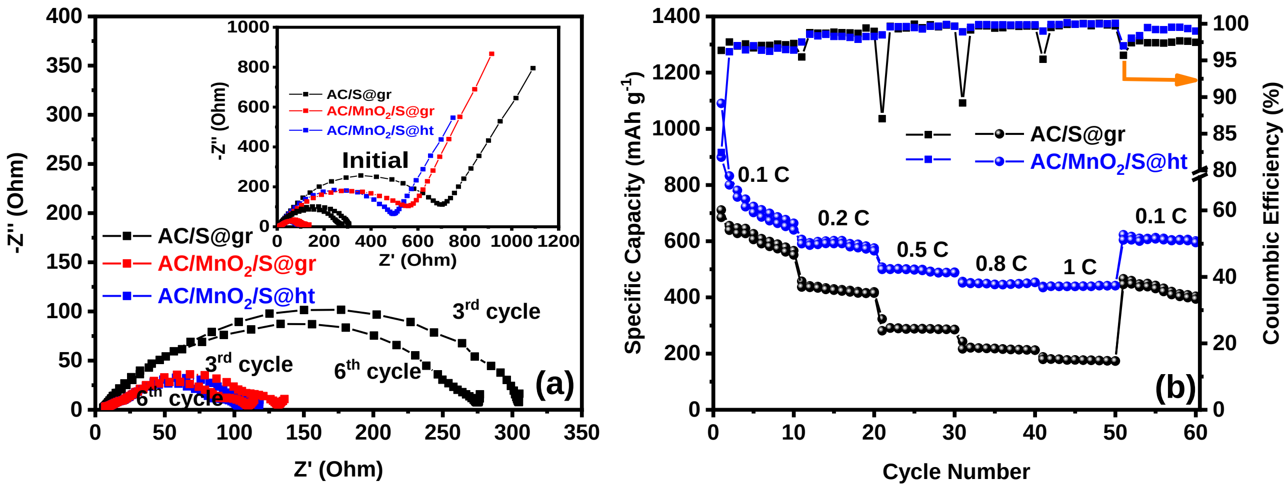
-Z'' (Ohm)
Z' (Ohm)
AC/S@gr
AC/MnO2/S@gr
AC/MnO2/S@ht
Initial
3rd cycle
6th cycle
(a)
Specific Capacity (mAh g-1)
Coulombic Efficiency (%)
Cycle Number
0.1 C
0.2 C
0.5 C
0.8 C
1 C
(b)

Figure 6.

Supplementary Materials

Click here to download Supplementary Materials: SUPPLEMENTARY INFORMATION (rev).docx